CCFE
CULHAM CENTRE FOR FUSION ENERGY

UK Atomic Energy Authority

UKAEA-CCFE-PR(20)130

A.Kareer, E. Tarleton, C. Hardie, S.V.Hainsworth,
A.J.Wilkinson

Localised deformation beneath Nanoscratch and Nanoindentation experiments

Localised deformation beneath Nanoscratch and Nanoindentation experiments

A.Kareer, E. Tarleton, C. Hardie, S.V.Hainsworth, A.J.Wilkinson

This is a preprint of a paper submitted for publication in
Acta Materialia

Localised deformation beneath Nanoscratch and Nanoindentation experiments

A.Kareer[a], E. Tarleton[b,a], C. Hardie[c,a], S.V.Hainsworth[d], A.J.Wilkinson[a]

[a]*Department of Materials, University of Oxford, Parks Road, Oxford, OX1 3PH, United Kingdom*
[b]*Department of Engineering Science, University of Oxford, Parks Road, Oxford, OX1 3PJ, United Kingdom*
[c]*Culham Centre for Fusion Energy, UK Atomic Energy Authority, Abingdon, OX14 3DB, United Kingdom*
[d]*Aston Institute of Materials Research, School of Engineering and Applied Science, Aston University, Aston, Birmingham, B4 7ET, United Kingdom*

Abstract

In this paper we investigate the residual deformation field in the vicinity of nano-scratch tests using two tip orientations in a (001) Cu single crystal. We compare the deformation with that from indentation, in an attempt to understand the mechanisms of deformation in tangential sliding. The lattice rotation fields are mapped experimentally using high-resolution electron backscatter diffraction (HR-EBSD) on cross-sections prepared using focused ion beam (FIB). A physically based crystal plasticity finite element model (CPFEM) is used to simulate the lattice rotation fields, in terms of the sense and axis, and offers insight into the 3D rotation field surrounding nano-scratch experiments, as it transitions from an initial static indentation to the formation of a steady-state scratch.

Keywords: Nanoindentation, Nanoscratch, HR-EBSD, CPFEM

1. Introduction

The extensive development of nanomechanical testing instruments has expanded the capabilities of nanoscale measurement beyond basic indentation hardness. Nanoscratch has generated significant interest and can be performed on commercial nanoindenters, requiring only minor adaptations to the software. When used in combination, nanoscratch and nanoindentation provide a powerful means to investigate the near surface mechanical and tribological properties of small volumes of material [1, 2, 3, 4]; it enables the study of nanoscale friction [5, 6] and allows the adhesive strength and fracture properties of coated systems to be characterised [7, 8, 9].

Macroscopically Tabor showed that on the basis of plastic deformation, there is a strong correlation between the indentation and scratch hardness when the measurement is based on a mean pressure [10]. As a consequence, the indentation hardness is the key metric used to define wear resistance [11]. The complex surface interactions involved in wear processes are extremely difficult to understand and simplified models such as this do not completely take into account the physical mechanics that are occurring. Nanoscratch testing has the advantage, in that it provides an experimental platform to reproduce a single point, sliding asperity contact, that is believed to control the process of abrasive wear [4, 12, 13]. Hence, it is becoming increasingly common to use this technique to study the near surface mechanical properties via determination of the scratch hardness, from which the wear resistance of material systems can be inferred [14, 15, 16, 17]. The remaining issue resides in the definition of scratch hardness; the simplest and most frequently used measurement of scratch hardness is analogous to indentation hardness and is defined as the ratio between the normal load and the projected load bearing area. The studies that have used this

definition, show substantial differences between the measured indentation and scratch hardness [18, 19, 20]. By further incorporating the lateral force into the measurement, it is possible to obtain a scratch hardness measurement that is in closer agreement to the indentation hardness, on isotropic materials [21, 22]. This however, is not applicable to all material classes, particularly metallic samples that exhibit work hardening and anisotropy, as shown in [23, 24]. A number of critical considerations must additionally be accounted for; namely the effect of adhesion, plasticity size effects, the resultant strain on the material, work hardening as a result of evolving dislocation structure and the direction of flow of displaced material in each loading direction [15]. In order to interpret the differences measured in indentation and scratch hardness, it is important to develop a deeper understanding of the mechanics of nanoscratch formation.

Experimental observations of the deformation field beneath indentation experiments, have been used to interpret the hardening behaviour in various materials. These studies have revealed that the plastic zone is extremely complex and there is a continued effort to relate the deformation field to the measured mechanical properties [25, 26, 27, 28, 29]. Several studies have reported that for indentation with a geometrically self-similar indenter, the geometrically necessary dislocation (GND) structure does not develop in a self-similar, hemispherical way as often assumed in simplified explanations [30, 31, 32]. The lattice rotation fields below indentation experiments with various tip geometries, have revealed distinct patterning within the plastic zone that exhibit well defined boundaries and a steep orientation gradient where a change in the sign of the rotation direction is observed [25, 33, 34]. The investigation of plastic deformation and induced lattice rotations is of great interest for an improved micromechanical understanding of indentation experiments owing to the close connection between crystallographic shear and the resulting lattice rotation.

Simulation methods, such as the Crystal Plasticity Finite Element Method (CPFEM), provide further insight into the mechanics of the deformation field, when applied in conjunction with indentation experiments [35]. Through incorporation of an appropriate, physically based, constitutive model along with details of the microstructure and constitutive parameters, CPFEM enables the effect of grain size, crystallographic orientation [36] and plasticity size effects [37] to be studied. Zaafarani and co-workers simulated the lattice rotation field below spherical indentations in copper using CPFEM, and directly compared the simulated rotation fields with that obtained from EBSD [34]. Simulating the lattice rotation field allowed appropriate interpretation of the deformation mechanisms, by separating the crystallographic shear occurring on individual slip systems, and directly relating it to the patterns observed in the lattice rotation fields [38]. CPFEM has the added benefit in that it offers information on the spatial 3D distribution of the deformation field, in real time, as it evolves throughout the experiment. This is necessary to interpret dynamic experiments, whereby experimentally it is only possible to study a snapshot of the final, deformed state via postmortem analysis.

In comparison to nanoindentation experiments, the study of deformation below nanoscratch experiments is still in its infancy. The strain field is further complicated due to the lateral force. Macroscopic scratch experiments show that plastic deformation induces changes in the microstructure of the material, resulting in a distinct discontinuity between a surface layer and the underlying bulk material [39, 40, 41, 42, 43, 44]. This physical boundary has also been identified in TEM studies around nanoscratch experiments in Ni_3Al where the plastic zone consists of a core region with high dislocation density surrounded by an outer region with lower dislocation density [45].

Simplified mechanistic models have been proposed to simulate the plasticity dominated deformation field around nanoscratch experiments similar to those used for nanoindentation that assume the plastic zone is proportional to the scratch width [20, 46] but these models are purely theoretical and, in most cases, are not validated. Isotropic Finite Element models have been used to simulate the strain field around nanoscratch experiments in

an attempt to validate analytical models [47, 48] and to describe the strain field in both bulk and coated systems [49, 50]. A model by Holmberg and co-workers found that the stress field under scratch experiments in coated systems is different to that under bulk samples. This was attributed to the mismatch between material properties in the coating and substrate, which restricted the ability for the residual stresses to elastically recover. In the absence of a coating, elastic recovery is accommodated, resulting in a different stress field [51]. However, a detailed study of the effect of crystallographic orientation and the resulting lattice rotation field in the vicinity of nanoscratch experiments remains unexplored.

In this paper, we use High resolution EBSD (HR-EBSD) to experimentally map the lattice rotation field in the vicinity of nanoindentation and nanoscratch experiments [32, 52, 53, 54, 55]. Scratch and indentations were generated under the same normal force (3mN) using a Berkovich indenter, in single crystal copper. A physically based CPFE model is used to simulate the scratch experiment. Lattice rotation fields from the simulation are directly compared with the experimental results and provide an insight into the three-dimensional mechanisms that occur during deformation beneath a sliding contact which can help understand the quantitative differences observed between indentation and scratch hardness.

2. Methods

2.1. Nanoscratch and nanoindentation

Nanoscratch and nanoindentation experiments were carried out on a sample of single-crystal, oxygen-free pure copper with 99.9% purity, oriented in the (001) crystallographic plane (obtained from Goodfellow UK). The sample was annealed in air for 4 hours at 600°C, followed by a mechanical and electrolytic polish in order to obtain a smooth flat surface, with negligible residual stresses. The indentation and scratches were made using a Keysight (formerly Agilent, formerly MTS) G200 instrumented indentation system, fitted with a lateral force measurement probe and a Berkovich diamond tip; the scratches were formed in both the edge forward (EF) and face forward (FF) tip orientation, parallel to the [100] direction (corresponding to the x_1 direction in Figure 1(b)) at a velocity of 10 μm s^{-1}. The indentation had maximum load of 3mN. A constant normal force of 3 mN, was used for the scratches and a three-pass scratch method was used to correct the data for surface roughness and sample tilt. The corrected penetration depth channel is plotted as a function of scratch distance in Figure 1(a). Full details of the scratch method are provided in [24].

2.2. Cross-sectioning

Cross-sections through the nanoindentation and the scratch were prepared using a Zeiss Auriga FIB-SEM. Cross-sections were taken from two locations in the scratch; scratch section A is cut across the centre of the scratch and scratch section B is cut at the end of the scratch (these locations are shown in Figure 1 b). The indent section was taken from the centre of the indentation, in the same orientation as the scratch such that the cross-sectioned surface was oriented in the (100) crystallographic plane. Cross-sectional slices, of approximately $20\mu\text{m} \times 10\mu\text{m} \times 3\mu\text{m}$ in size, were lifted from the sample in-situ and mounted on an Omniprobe TEM copper grid. SEM images of the prepared cross-sections, prior to lift-out, are given in Figures 1(c) and 1(d).

2.3. High Resolution Electron Backscatter Diffraction

EBSD measurements of the cross-sections and surface of the scratches were made in a Zeiss Merlin FEG SEM equipped with a Bruker e$^-$Flash$^{\text{HR}}$ EBSD detector operated by Esprit 2.0 software. The EBSD patterns (EBSPs) were acquired using an electron beam energy of 20kV and a probe current of 5nA; a step size of 50nm was used and EBSPs were collected and saved at a resolution of 800×600 pixels.

HR-EBSD is used to map the lattice rotation field in the vicinity of the indentation and scratch experiments. The technique uses an image cross-correlation based analysis to measure the lattice curvature within the crystal. A reference pattern is selected from a location within

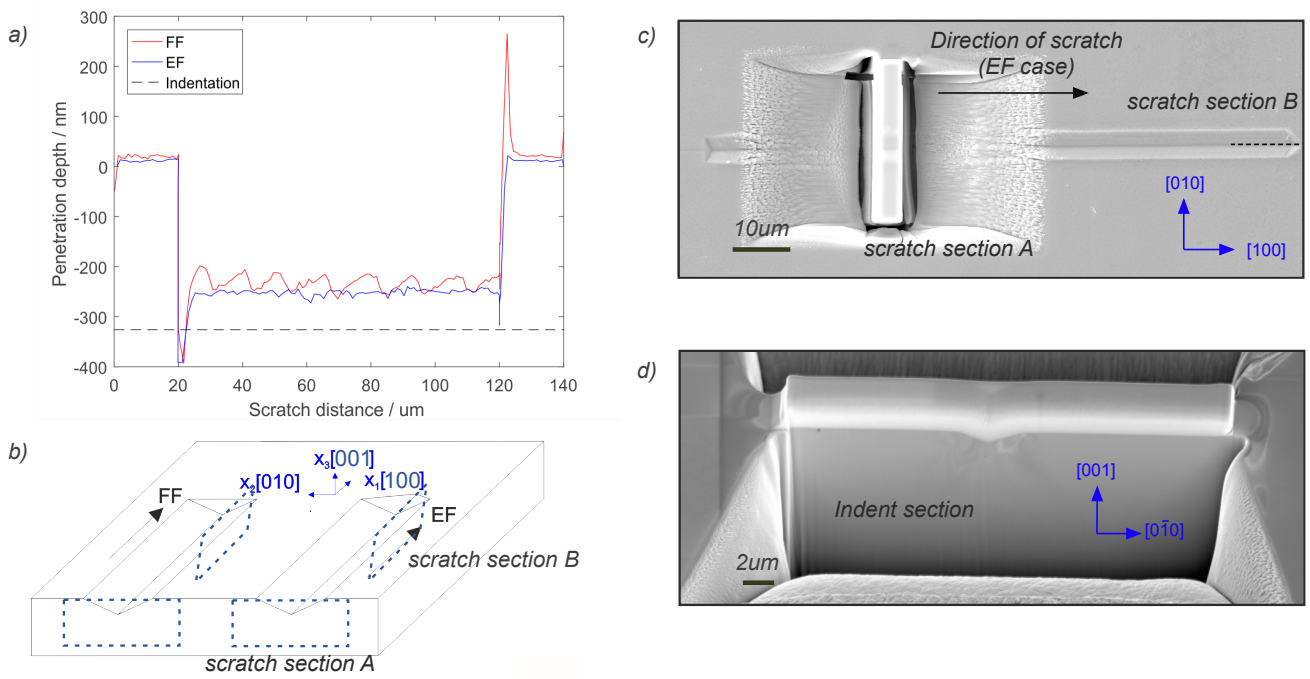

Figure 1: a) Raw experimental penetration depth vs. scratch distance for FF and EF scratch. b) Schematic of the scratch directions with respect to the crystallographic orientation and location of sections lifted for EBSD analysis. c) SEM image of EF scratch and FIB prepared scratch section A d)SEM of FIB prepared indent section.

the grain far from the regions of high deformation (in the case of the single crystal used in this study, the reference pattern is selected far from the indented/scratched region of the orientation map). Each test pattern within the map is cross-correlated with respect to the reference pattern; the pattern shifts of a number of regions of interest (ROIs) are measured and related to the crystal lattice rotation. A full description of the mathematics describing the method can be found here [52, 53, 54]. Lattice rotations between test and reference pattern can be used to estimate the GND density based on Nyes framework [56, 52]. The total dislocation density comprises individual dislocation densities from each dislocation slip system. For an FCC crystal it is assumed that the GNDs are either pure screw dislocations, or pure edge dislocations with $\langle 110 \rangle$ Burgers vectors giving 18 types of unknown dislocation densities. Cross-correlation of a 2D EBSD map allows the lattice rotation tensor to be determined in the plane of the measured surface giving six out of the nine lattice rotation tensor components. At each point in the map, a set of possible GND combinations that satisfy the six measured lattice curvatures are found and the combination that gives the minimum total line energy is chosen. Further information can be found in [32]. For the experimental conditions used, this method measures lattice rotations with an angular sensitivity of 3×10^{-4} rad which corresponds to a lower bound GND density noise floor of $1.5 \times 10^{13} m^{-2}$.

2.4. Crystal plasticity finite element modelling

Finite element simulations were performed using Abaqus 2016 to investigate the influence of deformation due to scratching with the EF tip geometry, in single crystal copper. A crystal plasticity user material (UMAT) for Abaqus was used based on the user element (UEL) written by Dunne et al. [57, 35].

The deformation is decomposed multiplicatively

into a plastic, $\boldsymbol{F}^p$, and elastic, $\boldsymbol{F}^e$, deformation gradient

$$F_{ij} = F^e_{ik} F^p_{kj} \tag{1}$$

the flow rule has the form

$$\dot{F}^p_{ij} = L^p_{ik} F^p_{kj}. \tag{2}$$

Where the plastic velocity gradient, $\boldsymbol{L}^p$, is given by the crystallographic strain rate resulting from dislocation glide on the active slip systems with slip direction $\boldsymbol{s}^k$ and slip plane normal $\boldsymbol{n}^k$

$$L^p_{ij} = \sum_{k=1}^{k=12} \dot{\gamma}^k(\tau) s^k_i n^k_j \tag{3}$$

The crystallographic slip rate $\dot{\gamma}$ is given by

$$\dot{\gamma}^k(\tau) = A \sinh\left(B(|\tau^k| - \tau_c)\right) \operatorname{sgn}(\tau^k) \tag{4}$$

for $|\tau^k| > \tau_c$ and $\dot{\gamma}^k = 0$ otherwise, where the resolved shear stress on slip sytem k is $\tau^k = \sigma_{ij} n^k_i s^k_j$. The critically resolved shear stress is assumed the same for each slip system,

$$\tau_c(\rho) = \tau^0_c + C\mu b\sqrt{\rho}. \tag{5}$$

For simplicity we assume that the dislocation density, ρ is proportional to the plastic strain

$$\dot{\rho} = D\sqrt{\frac{2}{3}\dot{\varepsilon}^p_{ij}\dot{\varepsilon}^p_{ij}} \tag{6}$$

where the plastic strain rate $\dot{\varepsilon}^p_{ij}$ is the symmetric part of L^p_{ij}. The fitting constants were $A = 10^{-6}$ s^{-1}, $B = 0.1$ MPa^{-1}, $C = 0.05$ and $D = 2.45 \times 10^4 \mu\mathrm{m}^{-2}$. Consequently plastic deformation induces a dislocation density which hardens the slip systems via an increase in the CRSS, $\tau_c(\rho)$.

A total of 4950 linear elements with 8 Gauss points per element (C3D8) were used to represent a block of copper with dimensions of L = 25×15 × 7.5 μm, with symmetry boundary conditions were applied along the (010) mid plane allowing only half of the domain to be simulated. The scratch test was simulated by modelling an indent followed by an edge forward (EF) scratch step with a constant displacement of $u_3 = 247$ nm and applied lateral displacement of $u_1 = 10$ μm at a rate of 10 μm/s. A scratch length of 10 μm was found to be sufficient to reach a steady state scratch formation. A biased mesh under the scratch was used with an approximate element size of $w_1 = 0.4$ μm along the scratch direction u_1, $w_2 = 0.2$ μm along u_2, increasing up to $w_2 = 1$ μm far away from the scratch. The indenter tip was modelled as a rigid part with a perfect Berkovich geometry. The finite sliding, node to surface, Abaqus contact algorithm was used with the default hard contact property. The absolute values for the lateral and normal force are determined by the material model however, their ratio is governed entirely by the friction behaviour. A friction coefficient of 0.15 was used to specify tangential behaviour between the surfaces in contact. This value was calculated from the experimental data by resolving the normal, F_N, and tangential forces, F_T, on the indenter tip faces during sliding; where the friction coefficient is $\mu_f = F_T/F_R$. Full details of the friction coefficient calculation are provided in Appendix A.8. The symmetry plane was fixed from translation in the normal direction,$u_2 = 0$, the nodes on the top surface were traction free, while the remaining four surfaces of the cube were fixed. Elastic anisotropy was used with the following elastic constants for copper $E = 66$ GPa, $G = 75$ GPa, and $\nu = 0.42$ and 12 $\langle 1\bar{1}0\rangle\{111\}$ fcc slip systems were included with an initial CRSS of $\tau^0_c = 1$ MPa. Further details on the UMAT can be found in [58, 59, 60, 61, 62, 63]. Simulations provide details of the plastic deformation of the free surface around the EF scratch.

3. Results

The experimentally measured and simulated penetration depth, normal force and lateral force are given in Figure 2 for the EF tip orientation. Data from a scratch distance of 35 μm-60 μm are shown, where the experimental scratch had reached a steady state and the normal force was maintained at 3 mN without any influence of loading and unloading of the indenter. The simulated scratch data is presented for comparison. As the simulated scratch was only 10 μm long,

this is compared with the steady state region, between 40 μm-50 μm, of the experimental scratch data. The oscillations that appear in the simulated data are an artefact with a wavelength defined by the the node spacing w_1 and the initial 2μm can be interpreted as the settling in portion of the scratch. Once steady state scratch deformation is achieved, there is excellent agreement between the experimental and simulated normal and lateral forces.

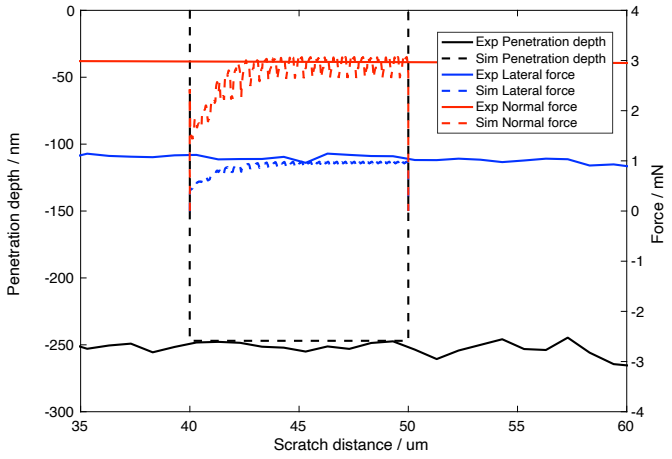

Figure 2: Penetration depth, normal force and lateral force vs. scratch distance between 35μm-60μm for experimental scratch. Simulated scratch data is presented between 40μm and 50μm

Lattice rotation fields, ω_{12}, ω_{13} and ω_{23} are shown in Figures 3-5. These fields correspond to rotations about the x_3, x_2 and x_1 axis respectively (the crystallographic orientation is shown in Figure 1(b)). The colour code represents the lattice rotation in radians; the scale has been confined to a magnitude of 0.03 radians (1.7°) to enable a clearer visualisation of the shape and sense of the rotation fields. Owing to a combination of edge effects, highly localised deformation and milling-induced curvature, there was insufficient overlap between the captured EBSD patterns and the reference pattern in regions closest to the surface of the indenter. As a result, HR-EBSD was unable to compute the lattice rotation fields in these regions. To indicate the exact surface of the sample, lattice rotation maps are overlaid on the greyscale image quality map from EBSD. Throughout this work, we refer to a positive lattice rotation as an anticlockwise rotation about the axis when looking towards the origin.

Figures 3(a)-(c) show the lattice rotation fields for the indentation cross section, measured experimentally using HR-EBSD. Figure 3(e)-(f) are the equivalent fields for the FF scratch cross section A (indicated in Figure 1) and Figures 3(g)-(i) are the corresponding fields from the EF scratch. Finally, Figures 3(j)-(k) show the corresponding simulated rotation fields for the EF scratch which was taken from a scratch distance of 5μm.

From the experimental maps, it is clear that the residual elastic rotation field below a scratch extends significantly further than beneath an indent created under the same normal force and that the FF scratch has a larger deformed region (plastic zone) than the EF scratch. The faceted Berkovich indenter creates a deformation field that takes a distinctive double-lobed form, with a steep maxima in the rotations in regions tangent to the indenter facets - the orientation of these facets with respect to the loading axis is different for each experiment and this is reflected in the shape of the plastic zone. In the indentation and EF oriented scratch, the double-lobe shape is more prominent, as these geometries have a sharp edge leading the deformation as opposed to the FF oriented scratch which has a flat facet driving the deformation.

In order to describe the rotation fields, it is assumed that material rotates about the apex of the indenter tip. The indentation field can be interpreted as the lattice rotating toward the apex of the indent for ω_{12} (Figure 3 a) and ω_{23} shows the rotation field is towards the free surface away from the indent (Figure 3 c) and down near the indent. Note that for the indentation, ω_{13} (Figure 3(b)) is dependent on the location of the section and although every effort was made to prepare this section across the centre of the indent, experimentally this is challenging and it is likely that it is slightly off centre.

The ω_{12} and ω_{13} rotation fields in both scratch experiments shows that the lattice rotates towards the indenter apex and towards the direction of which the scratch travels, i.e. along the positive x_1 direction, into the page. The in-plane rotation

field ω_{23} (Figure 3(f) and (i)) show that the lattice rotates away from the indenter apex towards the free surface, opposite to that observed for indentation. For the FF case (Figure 3(f) there is an inner region of counter rotation. This counter region can also be identified in the EF rotation field (Figure 3(i)) however it is not as obvious. In terms of the sense of rotation, the model is able to accurately simulate the experimentally observed deformation-induced rotation field, including the inner deformation zone of counter rotations. Although the simulated plastic zone size is smaller than the experiment, the double-lobed shape is simulated. The simulation also provides additional information regarding the lattice rotations close to the indenter apex, where experimental data could not be obtained.

Similar rotation field maps of the scratch surface are given in Figure 4 about the same axes. On the surface, the rotation fields correspond with that observed subsurface with a change in rotation sense either side of the scratch track in ω_{13} and ω_{23}) and a lattice rotation towards the direction of travel, [100], in ω_{13}. The scratch width is approximately 4μm, which corresponds with that in the simulation. Note that in Figure 4, the experimental scratch width appears wider due to to the lack of experimental HR-EBSD data close to the scratch edges. At the end of the scratch track there is considerable deformation from piled-up material. For the EF case, the sign of the in-plane rotation ω_{12} changes at the end of the scratch (Figure 4(d)). In Figure 5, which shows the experimental and simulated rotation fields from scratch section B, this is more obvious. As before with indentation, the rotation fields shown for scratch section B are dependent on the precise location of where cross section was prepared, and although the aim was to target the very centre of the scratch track, experimentally this is challenging and it is likely that the slice was taken slightly off centre. The exact offset for the experimental cross-section is unknown however it is assumed to be within the range of 50nm-200nm. Figures 5(g)-(i) show the simulated cross-sections offset by 100nm from the centre of the scratch for comparison. The discrepancy between the experimental and simulated ω_{12} rotation field is likely due to this uncertainty.

Figure 6 compares the experimental GND density field measured using HR-EBSD, with that of the total dislocation density, ρ_{total} calculated in the CPFE model:

$$\rho_{total} = \sum_{i=1}^{N} \dot{\rho}_i \Delta t_i \tag{7}$$

where $\dot{\rho}$ is defined in equation 6 for increment i, Δt_i is the increment time and N is the total number of increments. The magnitude and distribution of dislocation density calculated by the model is representative of that measured for the experiment, supporting the relatively simple definition of dislocation density evolution and associated hardening in the model. Compared to the modelling results, a larger plastic zone is observed in the experimental measurements of rotations and dislocation density fields surrounding the scratch. This difference may be the effect of the indenter tip being slightly rounded/blunt in the experiment which would displace more material than the perfect tip used in the model and/or heterogeneous material properties in the surface layer of the sample as a result of sample preparation induced damage.

4. Discussion

This work uses HR-EBSD to study the local deformation field around nanoscale experiments. The multiple views of the scratch rotation field, presented in the experimental results enables a more comprehensive investigation of the volume of deformed material surrounding the scratch. However, it remains limited to a snapshot, postmortem analysis and is not sufficient to the measure deformation in the regions where the largest rotations occur, close to the indenter apex. The 3-D rotation fields produced from simulation provide a real-time visualisation of the deformation field during scratch formation and are able to predict the deformation close to the indenter, where experimental data is missing. Hence in this work, the experiments and simulations were complementary to each other, and enabled a more complete

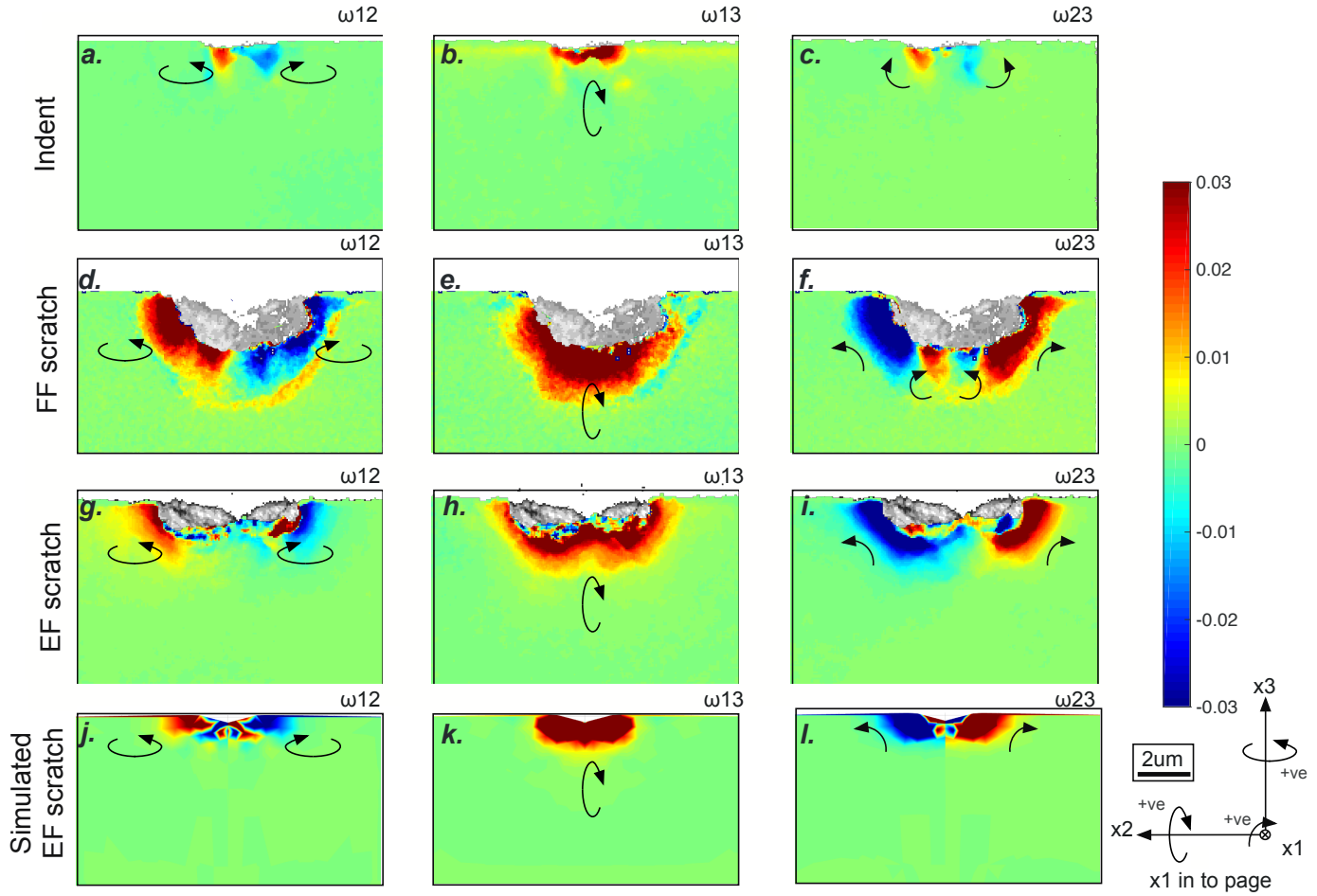

Figure 3: Lattice rotation field maps for the indent section and the scratch sections A about the x_3, x_2 and x_1 axis; ω_{12}, ω_{13} and ω_{23} respectively. a, b and c are rotation fields from the indent, d, e and f are the FF scratch cross section A rotation field, g, h and i are the EF scratch section A rotation field. j, k and l show the simulated rotation fields of the EF scratch section A. The colour code shows the lattice rotation in radians. Lattice rotation maps are overlaid on the greyscale image quality maps from EBSD. Scaling is identical for all diagrams.

investigation. The CPFE model was able to accurately predict the rotation field for the EF tip orientation in terms of sense and axis. The accurate prediction of the normal and lateral forces, relied on a correct coefficient of friction which was measured experimentally. The most commonly reported coefficient of friction for scratch tests uses the ratio between the lateral and normal force, however, this was not sufficient for the model. A coefficient of friction based on the resolved forces acting on the facets of the tip (see Appendix A) was used which was more physically appropriate as it was based on the geometry of the tip and the surfaces in contact.

The rotation fields can be summaried by the following. For indentation, the lattice rotates about the indenter apex towards the central indenter loading axis. This can be qualitatively understood in terms of the mass that must be displaced by the indenter from the material immediately below the indenter, towards the surface to create pile-up around the indent. The rotation fields ω_{12} and ω_{13} measured experimentally, suggest that the centre of the indent would be further along the x_1 axis, into the page of Figure 3(a),(b) and (c).

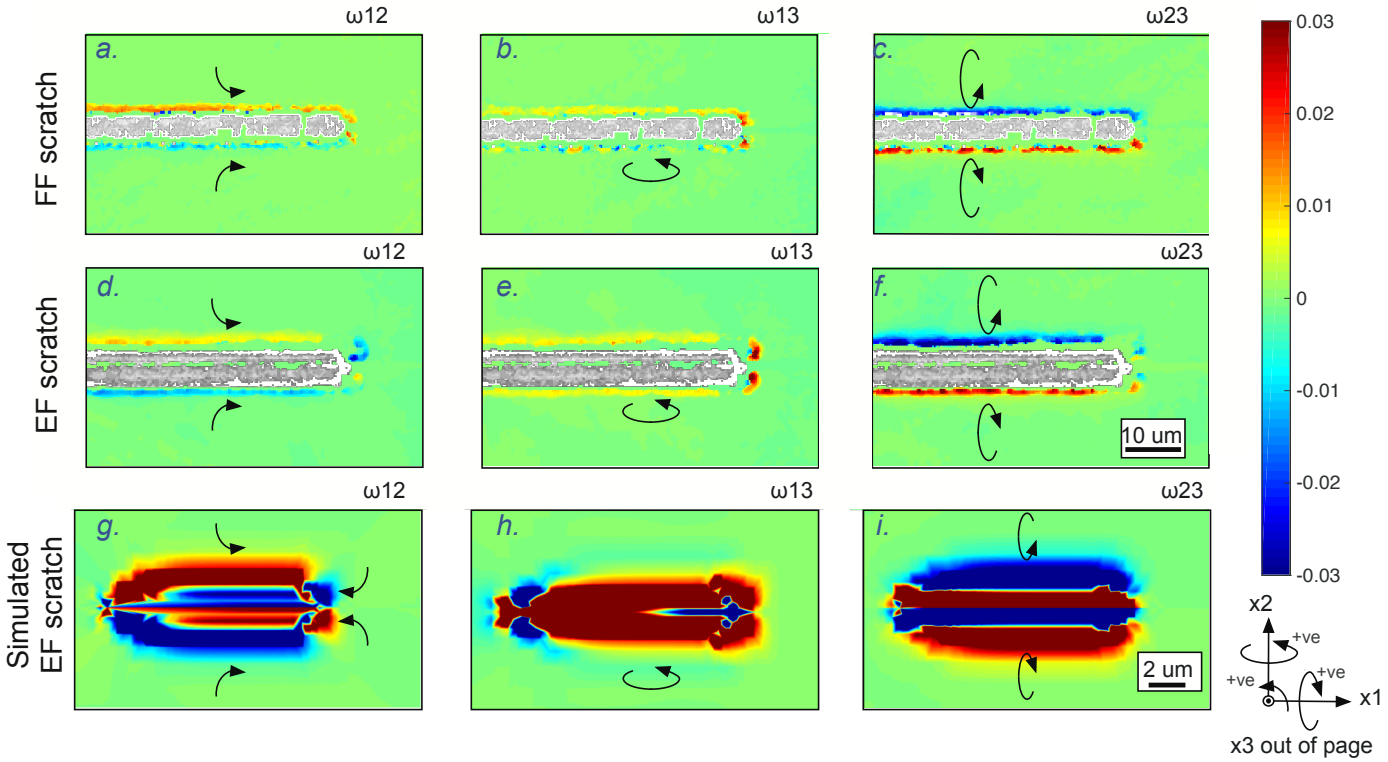

Figure 4: Lattice rotation field maps, experimental and simulated, of the surface about the x_3, x_2 and x_1 axis. Colour code shows the lattice rotation in radians. Lattice rotation maps are overlaid on the greyscale image quality maps from EBSD. Scaling is different between experiment and simulation, refer to scale bars.

The differences between the two scratch tip geometries in terms of the shape of the plastic zone might be explained in terms of the way the mass of material ahead of the indenter is displaced around the tip for each orientation. In the FF tip orientation, the most efficient way would be for material to move underneath the tip, whereas in the EF orientation the angled facets would assist displacement of material around the tip. The exact displacements are more complex and would involve multiple directions for both tip orientations however this simple analogy could describe the differences between the two scratch tip geometries.

The sign of the rotation fields around the scratch experiments broadly follow a similar pattern for both the EF and FF tip orientations and can be described by two simultaneous mechanisms. Firstly, the lattice rotates towards the direction in which the scratch travels, i.e. the [100] direction, as the indenter 'pulls' the surrounding lattice along with it in the direction it is traversing. This is observed in ω_{12} and ω_{13}. The second mechanism causes the lattice to rotate about the indenter away from the centre of the normal loading axis of the indenter, represented in the ω_{23} rotation field, which is the opposite sense to that observed in the indentation. This is the most striking difference observed between the indentation and scratch rotation fields in the experimental data.

As the simulation modelled an indentation step followed by the scratch step, analogous to the experiment, it is possible to investigate the mechanics of scratch formation, as the loading state transitions from a static indentation to a steady state scratch. Which will aid the interpretation of differences observed between the indentation and scratch experiments. In Figure 7, the simulated ω_{23} rotation field, for a set of successive planes throughout the scratch, parallel to the (100) plane (i.e. parallel to scratch section A) are given. Figure 7(a), where the indenter is solely under a nor-

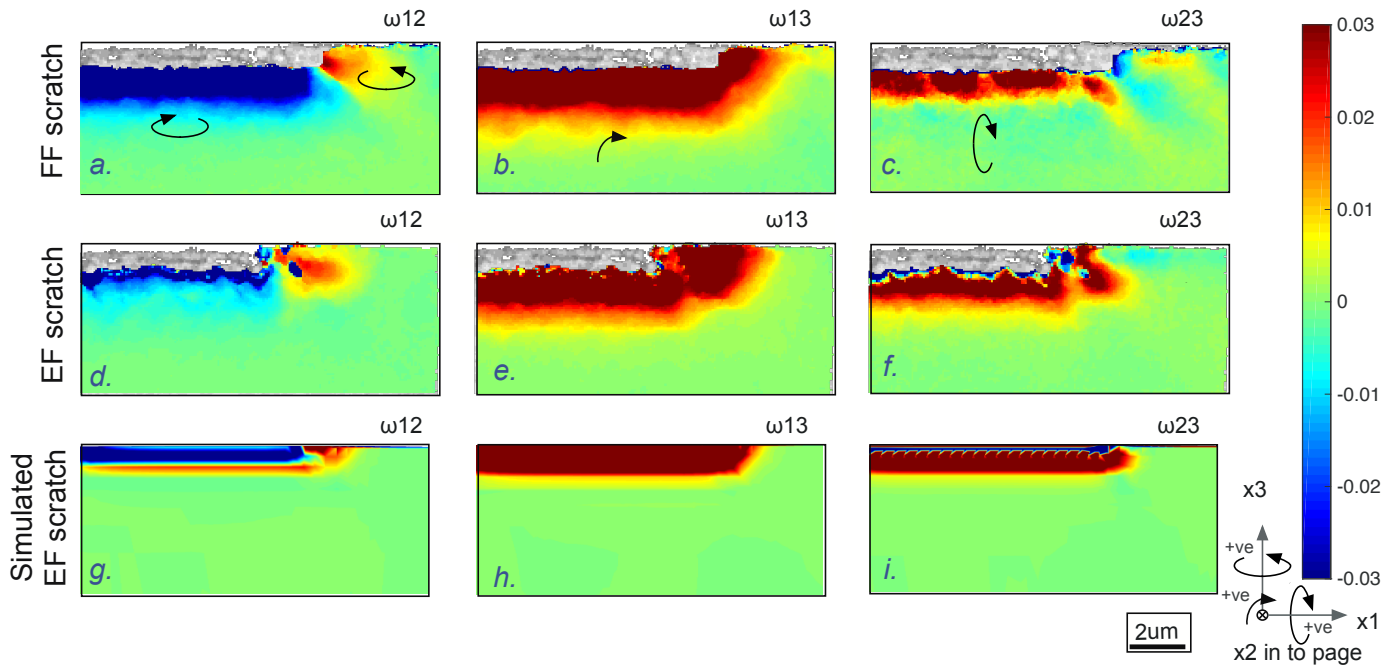

Figure 5: lattice rotation field maps for scratch section B about the x_3, x_2 and x_1 axis. The colour code shows the lattice rotation in radians. Lattice rotation maps are overlaid on the greyscale image quality maps from EBSD. Scaling is identical for all diagrams.

mal load (i.e. static indentation), shows a four-fold rotation field, where the zones close to the surface have the same rotation sense to that observed in the experimental indentation rotation (Figure 3(c). This four-fold rotation field has been observed for static indentations using a wedge indenter [64] and spherical indents [65, 58]. As the scratch begins to traverse laterally (Figure 7(b)), an additional outer region of counter rotation begins to develop at the surface, whilst the four-fold indentation rotation zone becomes further confined. As the scratch progresses, (Figure 7(c)-(f))the outer rotation zone expands further and dominates the plastic deformation field. It appears that in order to form a scratch, an additional shear stress is required to laterally move the inner zone of deformation, and generate an outer rotation field in the surrounding lattice. Referring back to the scratch displacement profile in Figure 1(a) it can be seen that in the early stages of the scratch formation, the displacement initially reaches a maximum of approximately 400nm, where the maximum normal force of 3mN is supported by the indentation alone. When the tip begins to traverse laterally, and the outer deformation field begins to form, the 3mN is only enough force to produce a displacement of 250nm. Hence the indenter rises up until it reaches a steady state displacement. Although the model uses a displacement controlled scratch step to aid numerical stability, the same mechanisms are observed in Figure 2. The initial indentation to a target depth of 247nm requires a normal force of 1.5mN, as the scratch progresses laterally, and the outer deformation field is formed, the normal force must increase in line with the experiment to maintain the constant penetration depth.

5. Conclusions

We present an investigation of the deformation field in the vicinity of a controlled scratch using a sharp (EF) and relatively blunt (FF) indenter orientation, in a Cu single crystal, for direct comparison with a static indentation. CPFE was used to simulate the experimental data and provide a more complete understanding of the nanoscratch formation. The main conclusions are as follows:

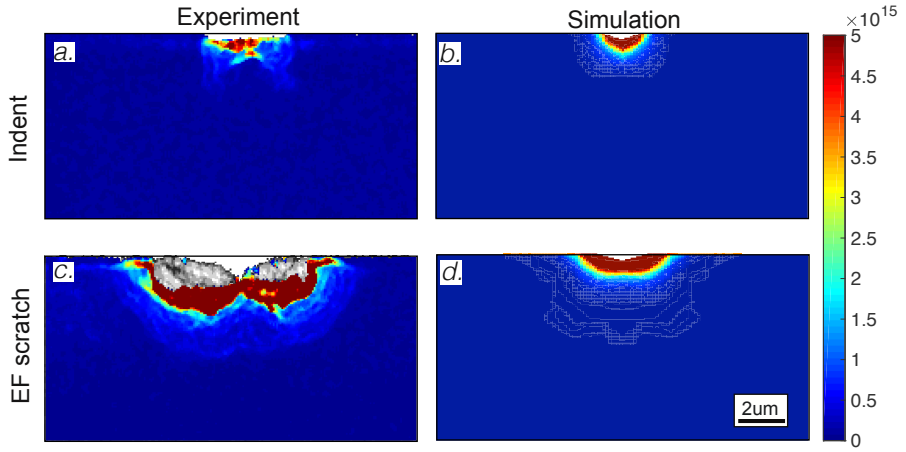

Figure 6: GND density map for the indent (a) and EF scratch section A (b) calculated experimentally using HR-EBSD. Corresponding total dislocation density from the CPFE simulation for the indent step (b) and the steady state scratch cross-section (d). Colour code shows the dislocation density per m^{-2}.

- By applying the same normal force, the three experiments show very different lattice rotation fields in terms of the shape and morphology.
- By simply incorporating lateral movement of the tip, an additional outer rotation zone, of opposite sense, forms in addition to the rotation field created by indentation alone. This implies that indentation, and therefore hardness does not fully capture the deformation associated with a sliding contact and may not be the most suitable metric to evaluate the wear resistance of a material. Scratch hardness could provide a more appropriate predictor.
- The commonly reported friction coefficient, $\frac{F_L}{F_N}$, is not specific to the geometry of the contact and therefore is not sufficient to use in the CPFE model to accurately predict the normal and lateral forces. A more appropriate coefficient is proposed.
- This work demonstrates the importance of a validated simulation to generate a deeper understanding of the mechanisms occurring in an experiment where only a post-mortem, 2-D snapshot can be analysed.

Acknowledgements

AK and ET acknowledges support from the Engineering and Physical Sciences Research Council under Fellowship grants EP/R030537/1 and EP/N007239/1 and Platform grant EP/P001645/1. CH also acknowledges funding by the UKRI Energy Programme (Grant No. EP/T012250/1).

Appendix A. Calculating the friction coefficient from experimental data

The coefficient of friction used in the model is given by Equation (A.1) where F_T is the tangential force parallel to the indenter facets and F_R is the resolved force perpendicular to the indenter facets (see Figure A.8). F_R and F_T are given by Equations (A.3) and (A.2) respectively for the EF tip geometry. The authors note an error in the equation for F_R presented in the appendix of [24] and A.3 is the correct expression.

$$\mu_f = F_T/F_R \tag{A.1}$$

$$F_T = \frac{F_L}{2}\cos\phi - \frac{F_N}{2}\sin\phi \tag{A.2}$$

$$\begin{aligned} F_R &= F_X\cos\theta + \frac{F_N}{2}\sin\theta \\ &= \frac{F_L}{4}\cos\theta + \frac{F_N}{2}\sin\theta \end{aligned} \tag{A.3}$$

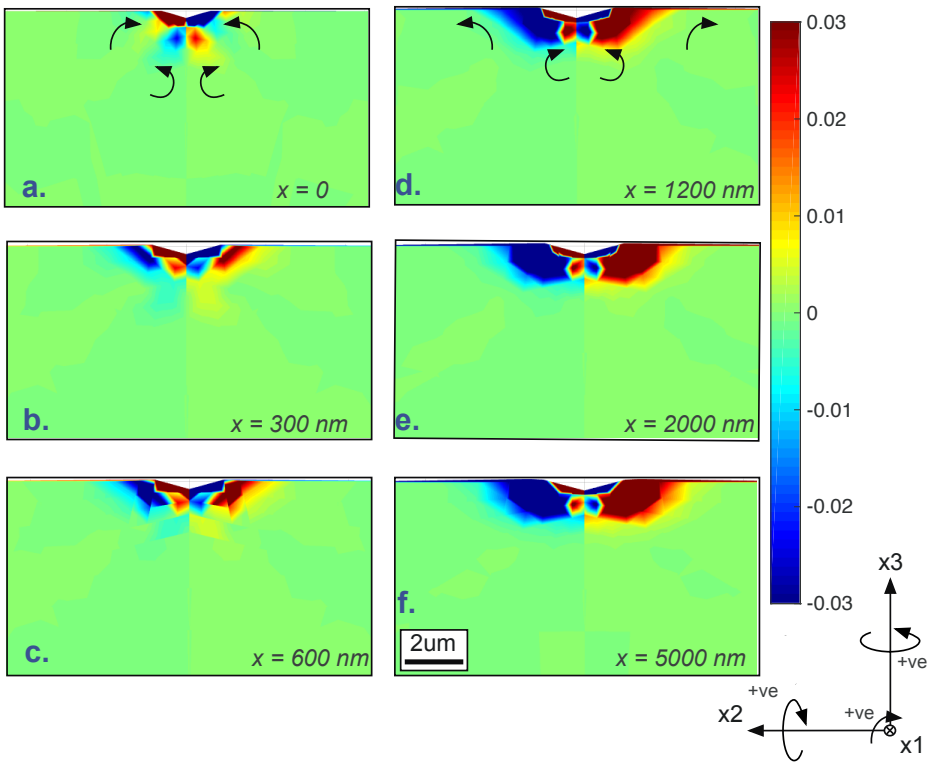

Figure 7: Simulated ω_{23} rotation field, for a set of successive planes through the scratch, parallel to the (100) plane (i.e. parallel to scratch section A). The colour code shows the lattice rotation in radians.

where $F_X = (F_L/2)\cos(60) = F_L/4$, $\theta = 65.3°$ and $\phi = 12.95°$ for a Berkovich indenter.

Whereas in in the face forward case (FF) the reaction and tangential forces are

$$F_R = F_L \cos\theta + F_N \sin\theta \qquad \text{(A.4)}$$

$$F_T = F_L \sin\theta - F_N \cos\theta \qquad \text{(A.5)}$$

and so the friction coefficient (A.1) becomes

$$\mu_f = \frac{\frac{F_L}{F_N}\tan\theta - 1}{\frac{F_L}{F_N} + \tan\theta} = \tan(\theta - \alpha) \qquad \text{(A.6)}$$

where $\alpha = \arctan(F_N/F_L)$

References

[1] J. Xia, C. Li, H. Dong, T. Bell, Nanoindentation and nanoscratch properties of a thermal oxidation treated γ-TiAl based alloy, Surface and Coatings Technology 200 (2006) 4755–4762.

[2] T. Tsui, G. Pharr, W. Oliver, C. Bhatia, R. White, S. Anders, A. Anders, I. Brown, Nanoindentation and nanoscratching of hard carbon coatings for magnetic disks, MRS Online Proceedings Library Archive 383 (1995).

[3] B. D. Beake, G. J. Leggett, Nanoindentation and nanoscratch testing of uniaxially and biaxially drawn poly (ethylene terephthalate) film, Polymer 43 (2002) 319–327.

[4] B. D. Beake, A. J. Harris, T. W. Liskiewicz, Review of recent progress in nanoscratch testing, Tribology - Materials, Surfaces & Interfaces 7 (2013) 87–96.

[5] S. Lafaye, M. Troyon, On the friction behaviour in nanoscratch testing, Wear 261 (2006) 905–913.

[6] B. Bhushan, J. A. Lowry, Friction and wear studies of various head materials and magnetic tapes in a linear mode accelerated test using a new nano-scratch wear measurement technique, Wear 190 (1995) 1–15.

[7] S. V. Hainsworth, S. J. Bull, T. F. Page, Scratch deformation response of thin cnx coatings at ultra-low loads, MRS Proceedings 522 (1998) 433.

[8] T. H. Zhang, Y. Huan, Nanoindentation and nano-scratch behaviors of dlc coatings on different steel substrates, Composites Science and Technology 65 (2005) 1409–1413.

[9] S.-Y. Chang, S.-Y. Lin, Y.-C. Huang, C.-L. Wu, Mechanical properties, deformation behaviours and interface adhesion of (AlCrTaTiZr)Nx multi-component coatings, Surface and Coatings Technology 204 (2010) 3307 – 3314.

[10] D. Tabor, The physical meaning of indentation and scratch hardness, British Journal of Applied Physics

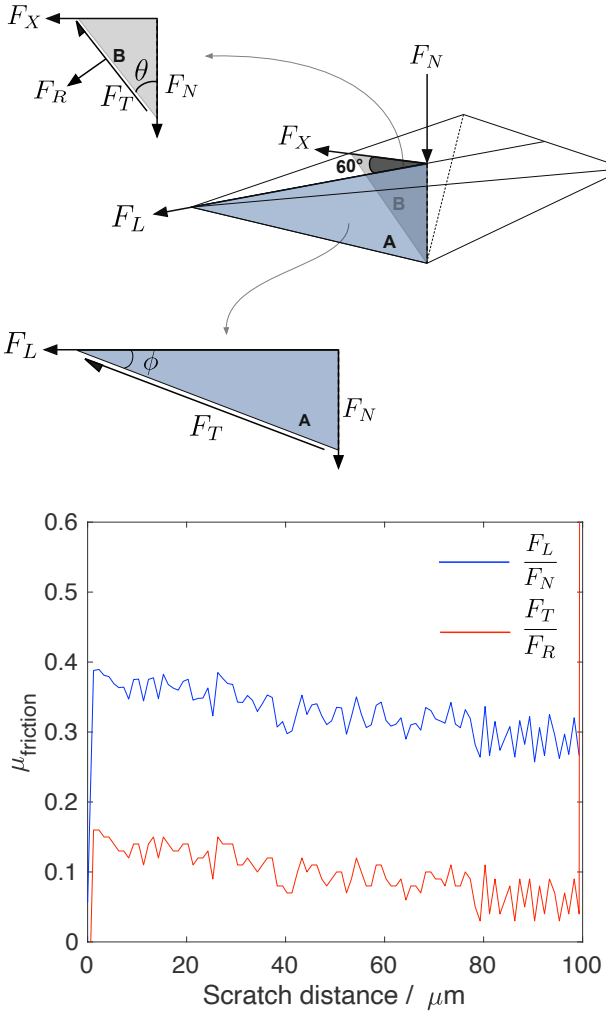

Figure A.8: Top: Schematic of indenter indicating forces acting on the facets. Bottom: Friction coefficient as a function of scratch distance using traditional and new definition

7 (1956) 159–166.

[11] J. Archard, Friction between metal surfaces, Wear 113 (1986) 3–16.

[12] S. R. Bakshi, A. K. Keshri, A. Agarwal, A comparison of mechanical and wear properties of plasma sprayed carbon nanotube reinforced aluminum composites at nano and macro scale, Materials Science and Engineering A 528 (2011) 3375–3384.

[13] S. P. Hutchings, I M, Triblology: Friction and wear of engineering materials, CRC Press, London (1992) 273.

[14] S. Graça, R. Colaço, R. Vilar, Micro-to-nano indentation and scratch hardness in the Ni–Co system: Depth dependence and implications for tribological behaviour, Tribology Letters 31 (2008) 177.

[15] C. A. Brookes, P. Green, P. H. Harrison, B. Moxley, Some observations on scratch and indentation hardness measurements, Journal of Physics D: Applied Physics 5 (1972) 1284–1293.

[16] S. J. Bull, E. G. Berasetegui, An overview of the potential of quantitative coating adhesion measurement by scratch testing, Tribology International 39 (2006) 99 – 114. 180 Years of Scratch Testing.

[17] C. A. Schuh, T. G. Nieh, T. Yamasaki, Hallpetch breakdown manifested in abrasive wear resistance of nanocrystalline nickel, Scripta Materialia 46 (2002) 735 – 740.

[18] N. Maan, A. B. V. Groenou, Low speed scratch experiments on steels, Wear 42 (1977) 365 – 390.

[19] A. S. Useinov, S. S. Useinov, Scratch hardness evaluation with in-situ pile-up effect estimation, Philosophical Magazine 92 (2012) 3188–3198.

[20] J. A. Williams, Analytical models of scratch hardness, Tribology International 29 (1996) 675–694.

[21] N. Tayebi, T. F. Conry, A. A. Polycarpou, Determination of hardness from nanoscratch experiments: Corrections for interfacial shear stress and elastic recovery, Journal of Materials Research 18 (2003) 21502162.

[22] N. Tayebi, T. F. Conry, A. A. Polycarpou, Reconciliation of nanoscratch hardness with nanoindentation hardness including the effects of interface shear stress, Journal of Materials Research 19 (2004) 33163323.

[23] A. Kareer, X. D. Hou, N. M. Jennett, S. V. Hainsworth, The existence of a lateral size effect and the relationship between indentation and scratch hardness in copper, Philosophical Magazine (2016) 1–18.

[24] A. Kareer, X. D. Hou, N. M. Jennett, S. V. Hainsworth, The interaction between Lateral size effect and grain size when scratching polycrystalline copper using a Berkovich indenter, Philosophical Magazine 6435 (2016) 1–16.

[25] Y. Zhang, N. Yunhe, L. Gao, Lattice rotation caused by wedge indentation of a single crystal: Dislocation dynamics compared to crystal plasticity simulations, Journal of the Mechanics and Physics of Solids 68 (2014) 267–279.

[26] D. Kiener, R. Pippan, C. Motz, H. Kreuzer, Microstructural evolution of the deformed volume beneath microindents in tungsten and copper, Acta Materialia 54 (2006) 2801–2811.

[27] J. W. Kysar, Y. X. Gan, T. L. Morse, X. Chen, M. E. Jones, High strain gradient plasticity associated with wedge indentation into face-centered cubic single crystals: Geometrically necessary dislocation densities, Journal of the Mechanics and Physics of Solids 55 (2007) 1554–1573.

[28] Y. F. Gao, B. C. Larson, J. H. Lee, L. Nicola, J. Z. Tischler, G. M. Pharr, Lattice Rotation Patterns and Strain Gradient Effects in Face-Centered-Cubic Single Crystals Under Spherical Indentation, Journal of Applied Mechanics 82 (2015) 061007.

[29] E. Demir, D. Raabe, N. Zaafarani, S. Zaefferer, In-

vestigation of the indentation size effect through the measurement of the geometrically necessary dislocations beneath small indents of different depths using EBSD tomography, Acta Materialia 57 (2009) 559–569.

[30] M. Rester, C. Motz, R. Pippan, Where are the geometrically necessary dislocations accommodating small imprints?, J. Mater. Res 24 (2009) 648.

[31] M. Rester, C. Motz, R. Pippan, Microstructural investigation of the volume beneath nanoindentations in copper, Acta Materialia 55 (2007) 6427–6435.

[32] A. J. Wilkinson, D. Randman, Determination of elastic strain fields and geometrically necessary dislocation distributions near nanoindents using electron back scatter diffraction, Philosophical Magazine 90 (2010) 1159–1177.

[33] M. Demiral, A. Roy, T. El Sayed, V. V. Silberschmidt, Influence of strain gradients on lattice rotation in nano-indentation experiments: A numerical study, Materials Science and Engineering A 608 (2014) 73–81.

[34] N. Zaafarani, D. Raabe, R. N. Singh, F. Roters, S. Zaefferer, Three-dimensional investigation of the texture and microstructure below a nanoindent in a Cu single crystal using 3D EBSD and crystal plasticity finite element simulations, Acta Materialia 54 (2006) 1863–1876.

[35] F. P. E. Dunne, R. Kiwanuka, A. J. Wilkinson, Crystal plasticity analysis of micro-deformation, lattice rotation and geometrically necessary dislocation density, Proceedings of the Royal Society A: Mathematical, Physical and Engineering Sciences 468 (2012) 2509–2531.

[36] S. Kucharski, S. Stupkiewicz, H. Petryk, Surface Pile-Up Patterns in Indentation Testing of Cu Single Crystals, Experimental Mechanics 54 (2014) 957–969.

[37] M. Liu, C. Lu, A. K. Tieu, Crystal plasticity finite element method modelling of indentation size effect, International Journal of Solids and Structures 54 (2015) 42–49.

[38] N. Zaafarani, D. Raabe, F. Roters, S. Zaefferer, On the origin of deformation-induced rotation patterns below nanoindents, Acta Materialia 56 (2008) 31–42.

[39] C. Greiner, Z. Liu, L. Strassberger, P. Gumbsch, Sequence of Stages in the Microstructure Evolution in Copper under Mild Reciprocating Tribological Loading, ACS Applied Materials and Interfaces 8 (2016) 15809–15819.

[40] N. K. Sundaram, Y. Guo, S. Chandrasekar, Mesoscale folding, instability, and disruption of laminar flow in metal surfaces, Physical Review Letters 109 (2012) 1–5.

[41] P. A. Romero, T. T. Järvi, N. Beckmann, M. Mrovec, M. Moseler, Coarse graining and localized plasticity between sliding nanocrystalline metals, Physical Review Letters 113 (2014) 1–5.

[42] W. L. Li, N. R. Tao, Z. Han, K. Lu, Comparisons of dry sliding tribological behaviors between coarse-grained and nanocrystalline copper, Wear 274-275 (2012) 306–312.

[43] A. Emge, S. Karthikeyan, D. A. Rigney, The effects of sliding velocity and sliding time on nanocrystalline tribolayer development and properties in copper, Wear 267 (2009) 562–567.

[44] M. S. Bednar, D. Kuhlmann-Wilsdorf, Amorphous and alloy film formation in sliding of silver on copper, Wear 183 (1995) 922–937.

[45] P. C. Wo, I. P. Jones, TEM study of the deformation structures around nanoscratches, Philosophical Magazine 6435 (2008).

[46] P. Burnett, D. Rickerby, The scratch adhesion test: An elastic-plastic indentation analysis, Thin Solid Films 157 (1988) 233–254.

[47] K. M. Lee, C.-D. Yeo, A. A. Polycarpou, Relationship between scratch hardness and yield strength of elastic perfectly plastic materials using finite element analysis, Journal of Materials Research 23 (2008) 2229–2237.

[48] S. C. Bellemare, M. Dao, S. Suresh, Effects of mechanical properties and surface friction on elastoplastic sliding contact, Mechanics of Materials 40 (2008) 206–219.

[49] J.-L. Bucaille, E. Felder, Finite-element analysis of deformation during indentation and scratch tests on elastic-perfectly plastic materials, Philosophical Magazine A 82 (2002) 2003–2012.

[50] J. Perne, Experimental and simulative strain field investigation of nano-and microscratches on nanolaminated (cr, al) n coating, Thin Solid Films 573 (2014) 33–40.

[51] K. Holmberg, A. Laukkanen, H. Ronkainen, K. Wallin, S. Varjus, J. Koskinen, Tribological contact analysis of a rigid ball sliding on a hard coated surface: Part i: Modelling stresses and strains, Surface and Coatings Technology 200 (2006) 3793–3809.

[52] T. B. Britton, J. L. R. Hickey, Understanding deformation with high angular resolution electron backscatter diffraction (HR-EBSD), IOP Conference Series: Materials Science and Engineering 304 (2018) 012003.

[53] B. Britton, I. Holton, G. Meaden, D. Dingley, High angular resolution electron backscatter diffraction: measurement of strain in functional and structural materials, Microscopy and Analysis 27 (2013) 8–13.

[54] A. J. Wilkinson, T. B. Britton, J. Jiang, P. S. Karamched, A review of advances and challenges in EBSD strain mapping, IOP Conference Series: Materials Science and Engineering 55 (2014) 012020.

[55] J. Jiang, T. B. Britton, A. J. Wilkinson, The orientation and strain dependence of dislocation structure evolution in monotonically deformed polycrystalline copper, International Journal of Plasticity 69 (2015)

102–117.
[56] J. Nye, Some geometrical relations in dislocated crystals, Acta metallurgica 1 (1953) 153–162.
[57] F. P. E. Dunne, D. Rugg, A. Walker, Length scale-dependent, elastically anisotropic, physically-based HCP crystal plasticity: Application to cold-dwell fatigue in Ti alloys, International Journal of Plasticity 23 (2007) 1061–1083.
[58] A. J. Cackett, C. D. Hardie, J. J. Lim, E. Tarleton, Spherical indentation of copper: Crystal plasticity vs experiment, Materialia 7 (2019) 100368.
[59] N. Grilli, P. Earp, A. C. Cocks, J. Marrow, E. Tarleton, Characterisation of slip and twin activity using digital image correlation and crystal plasticity finite element simulation: Application to orthorhombic α-uranium, Journal of the Mechanics and Physics of Solids 135 (2020) 103800.
[60] N. Grilli, A. C. Cocks, E. Tarleton, Crystal plasticity finite element modelling of coarse-grained α-uranium, Computational Materials Science 171 (2020) 109276.
[61] W. Roberts, J. Gong, A. J. Wilkinson, E. Tarleton, Tension–compression asymmetry of <c+ a> slip in Ti–6Al, Scripta Materialia 178 (2020) 119–123.
[62] S. Das, F. Hofmann, E. Tarleton, Consistent determination of geometrically necessary dislocation density from simulations and experiments, International Journal of Plasticity 109 (2018) 18–42.
[63] M. P. Petkov, J. Hu, E. Tarleton, A. C. Cocks, Comparison of self-consistent and crystal plasticity fe approaches for modelling the high-temperature deformation of 316h austenitic stainless steel, International Journal of Solids and Structures 171 (2019) 54 – 80.
[64] J. W. Kysar, Y. X. Gan, T. L. Morse, X. Chen, M. E. Jones, High strain gradient plasticity associated with wedge indentation into face-centered cubic single crystals: geometrically necessary dislocation densities, Journal of the Mechanics and Physics of Solids 55 (2007) 1554–1573.
[65] Y. Gao, B. C. Larson, J. Lee, L. Nicola, J. Tischler, G. M. Pharr, Lattice rotation patterns and strain gradient effects in face-centered-cubic single crystals under spherical indentation, Journal of Applied Mechanics 82 (2015).